Defect-engineered TiO_2 nanotube cathode for nitrate reduction to ammonia and upcycling into $(NH_4)_2SO_4$ in the paired electrolysis system

Qi Zhang, Yifan Li [*], Mengnan Geng, Juntao Zhu, Haofen Sun, Bo Jiang [*]

School of Environmental and Municipal Engineering, Qingdao University of Technology, Qingdao 266033, PR China

ABSTRACT

Wastewater contains significant amounts of NO_3 that can be directly electrochemically upcycled into the valuable ammonia products. In this study, based on the density functional theory, a defect-engineered TiO_2 nanotube array cathode (Co-BTNA) was developed for NO_3 reduction and further upcycling into $(NH_4)_2SO_4$ in the paired electrolysis system. The doped cobalt and oxygen vacancy defects in the Co-BTNA synergistically facilitated the electrons transfer to NO_3 with high selectivity of NH_3. Meanwhile, the acid anolyte produced via the electrochemical half-reaction at anode was used to trap NH_3 for $(NH_4)_2SO_4$ production. At a current density of 18 $mA \cdot cm^{-2}$, 100 % of NO_3 removal efficiency and 93.0 % of NH_3 selectivity were achieved with NH_3 recovery rate of 182.25 $g \text{-}(NH_4)_2SO_4 \cdot d^{-1} \cdot g_{cat}^{-1}$ at energy consumption of 27.1 $kWh \cdot kg^{-1}(NH_4)_2SO_4$. In general, this study proposed a sustainable and efficient approach for upcycling wasted NO_3 into ammonia fertilizer without external acid and alkali addition.

1. Introduction

The food and agriculture organization of the united nations (FAO) estimates that about 117 million tons of ammonia fertilizers are used in agriculture to maintain soil fertility and increase crop yields every year [1]. Currently, the ammonia fertilizer products mainly originate from the Haber-Bosch process that fixes N_2 with H_2 to produce ammonia (NH_3). But such an instrumental industry consumes approximately 2% of the global supply of energy to sustain the harsh reaction condition (temperature ~500 °C, pressure 150–300 bar), which accounts for around 1% of total emissions of the greenhouse gas [2]. Unlike N_2 with inert bond (941 $kJ \cdot mol^{-1}$), nitrate (NO_3), a common pollutant in wastewater, has relatively low binding energy (204 $kJ \cdot mol^{-1}$), which promises much better reaction kinetics for NH_3 production [3]. Particularly, diverse high-concentration industrial wastewater (such as metal finishing, nuclear fuel processing industries wastewater and waste brines from reverse osmosis and ion exchange [4–7]) provides abundant sources of NO_3 (e.g., 4–20 $g \text{-nitrogen} \cdot L^{-1}$) that could threat the ecological safety and human health if not properly treated [8]. Therefore, upcycling wasted NO_3 into value NH_3 fertilizers under ambient condition does not only hold the great premise to relieve energy crisis, but also help address environmental concerns [9].

Recently, sustainable NH_3 production by electrochemically reducing NO_3 (NRA) has attracted growing attention. Over the past few years, it has been made great strides in developing noble metal-based electrocatalysts (e.g., Ru, Pd, Pt, and Au) for NRA [10–12]. However, the high prices of these metals severely limit their large-scale applications in industry. TiO_2 nanotube array (TNA), which can be utilized directly as electrodes without additional adhesive substrates or organic binders, has shown great potential in electrochemical applications because of its high surface areas and especially the open-channel structure that facilitates mass transfer of the target substance [13]. Despite these advantages, the application of TNA in NRA is often restricted by its low electrical conductivity and poor selectivity to NH_3 [14]. Electrochemical reduction in aqueous electrolyte is an effective way to modulate the electronic properties of TNA and improve its conductivity [15], during which the oxygen vacancy (OV) defects can be created by removing the lattice oxygen atoms [14,16]. The resultant OVs in TNA served as active sites can efficiently capture and electrocatalytically reduce nitrate [17], but the NH_3 selectivity was still unsatisfied [18].

Doping transition metal atoms is also an effective defect-engineering strategy as those exotic atoms that interstitial or substitutional doped into the material lattice could trigger the lattice distortion, which can further increase the specific reaction rate by modulating the electronic structure and achieving polymetallic synergy [19,20]. Cobalt (Co) is considered one of the most effective doping species due to its abundant

electronic states [21]. For instance, Co-doped $FePS_3$ nanosheets reported to exhibit a remarkable electrocatalytic performance toward electrochemical ammonia synthesis, in which doping Co enhances the catalytic activities of Fe-edge sites, realizing a high NH_3 yield rate of 90.6 $\mu g\ h^{-1}$ mg_{cat}^{-1} [22]. Additionally, the introduction of cobalt into TNA have demonstrated can both create and stabilize surficial OVs, which significantly improve the electronic conductivity and catalytic activity for peroxymonosulfate activation [20]. Considering that Co-based electrocatalysts have demonstrated excellent NH_3 selectivity to NRA [23,24], we were inspired that the performance of TNA in NRA could be artificially designed and subtly modulated by defect engineering based on modifying TNA with the Co heteroatom and OV defect simultaneously, which however remains unexplored and challenging.

The electrochemically produced NH_3 from NO_3^- is considered as a value product only when it is successfully abstracted from its mother wastewaters. Otherwise, the produced NH_3 is a secondary pollutant and certainly deteriorates the water quality. Thus, the abstraction of NH_3 from wastewater is also a critical issue for electrochemically upcycling wasted NO_3^- into valuable ammonia products. Recently, in our previous study, isochronous NO_3^- reduction and NH_3 recovery was achieved by combining the NO_3^- reduction and membrane abstraction [25]. However, in this system, the electrochemical half-reaction at anode was only used to provide protons and electrons for NO_3^- reduction at cathode, and the acid anolyte was not used fully and discharged as wastewater after reaction. Instead, external acid (H_2SO_4) was added to capture the transferred gaseous NH_3 and generated $(NH_4)_2SO_4$, elevating the cost and hazardous risk. It is worth noting that utilizing the wasted oxygen evolution reaction at the anodic chamber to produce acids to absorb gaseous NH_3 into $(NH_4)_2SO_4$ can promise to solve this problem. Thus, optimizing the paired electrolysis between cathodic and anodic electrochemical half reactions could realize synchronous NO_3^- conversion to NH_3 and upcycling into $(NH_4)_2SO_4$ without the addition of acid/alkali, which is technically feasible in scientific and technological fields.

In this study, based on the directional defect engineering, a high-performance TNA cathode was directionally designed and fabricated by modified with the Co heteroatom and OV defect simultaneously for NRA. Systematical DFT investigations were applied initially to guide the subtly design of TNA catalysts. A series of TNA catalysts' structures (TNA, BTNA, Co-TNA and Co-BTNA) were constructed. And the individual as well as synergy contributions of Co doping and OV defects in enhancing the activity and NH_3 selectivity of Co-BTNA toward NRA were investigated in-depth in terms of electronic properties and reaction pathway analyses. Then, paired electrolysis and membrane abstraction were combined to achieve simultaneous $(NH_4)_2SO_4$ recovery without external acid and alkali addition. The influences of operation parameters and water matrices (working cathode potential, Cl^- concentration and NO_3^- concentration) on NO_3^- removal and NH_3 production were investigated.

2. Experimental section

2.1. Electrode preparation

The purchased Ti mesh (> 99.99%, thickness 1.2 mm, 5 × 5 cm) was first degreased by ultra-sonification in acetone, then cleaned by ultra-pure water, sonicated for 15 min, and dried for use. Self-organized amorphous TNA (am-TNA) on Ti mesh surface was obtained by anodization reaction at 42 V for 6 h in an ethylene glycol electrolyte containing 0.25 wt% NH_4F and 2 wt% H_2O [26]. After anodization, Am-TNA was subjected to a second anodization in 5 wt% H_3PO_4/ethylene glycol electrolyte at 42 V for 1 h to enhance its mechanical stability [14]. The doping of Co in am-NTA (Co/am-TNA) was carried out by dipping am-TNA into 250 mM $Co(NO_3)_2$ ethanol solution (100 mL) for 1 min and drying at room temperature for 2 min. The dipping process was repeated three times, and the TNA and cobalt-doped TNA (Co-TNA) were obtained after annealing am-TNA and Co/am-TNA in air at 450 °C

for 1 h, respectively. Finally, the oxygen vacancy-doped TNA (BTNA) and cobalt, oxygen vacancy co-doped TNA (Co-BTNA) were prepared by catharizing TNA and Co-TNA in 1 M $NaClO_4$ solution at a current density of 5 $mA\cdot cm^{-2}$ for 10 min

2.2. Material characterization and electrochemical tests

The crystalline phase was identified by X-ray diffraction measurement (XRD, Bruker D2 PHASER), and the 2θ ranged from 20° to 80°. Scanning electron microscopy (SEM, Zeiss, Model 1550VP) and transmission electron microscope (TEM, JEM-2100 F) were used to investigate the morphology of the nanotube electrodes. Energy dispersive spectroscopy (EDS) was used to measure the surface distribution of elements. The surface chemical composition was analyzed using the X-ray photoelectron spectroscopy (XPS, Thermo Fisher ESCALAB 250Xi) with Al Kα as an X-ray source. The Co loading and leaching amounts were determined by inductively coupled plasma atomic emission spectrometry (ICP-MS, Agilent 8800).

Electrochemical measurements were tested by an electrochemical workstation (CHI 660D, Chenhua, Shanghai). A typical H-type electrolytic cell separated by a proton exchange membrane (Dupont, Nafion 117) was employed. The prepared electrodes (1 × 1 cm), a saturated calomel electrode (SCE, +0.241 V vs. SHE), and a platinum foil were used as the working electrode, the reference electrode, and the counter electrode, respectively. The electrolyte for linear sweep voltammetry (LSV) and cyclic voltammetry (CV) tests was composed of 0.1 M Na_2SO_4 solution with or without 15 mM NO_3^-. LSV polarization curves were recorded at a scan rate of 0.1 $V\cdot s^{-1}$. Electrochemical double-layer capacity (C_{dl}) was determined via cyclic voltammetry (CV) at a scan rate (v) of 10–50 $mV\cdot s^{-1}$. The EIS plots were obtained over the frequency range of 30 kHz to 0.1 Hz by a potential amplitude of 5 mV. (Details in Supporting Information Part S2).

2.3. Operating parameter of the paired electrolysis cell

2.3.1. Electrocatalytic reduction of NO3- toward ammonia (ERNA)

The NO_3^- reduction was performed using an electrocatalytic NO_3^- reduction to NH_3 reactor (Fig. 1(a) and S1) with potential controlled by a potentiostat (CHI 660D, Chenhua, Shanghai) at room temperature (25 ± 1 °C) and ambient pressure. The reactor for electrocatalytic reduction of NO_3^- toward the ammonia (ERNA) consists of an anode chamber and a cathode chamber, with IrO_2-RuO_2/Ti and SCE as the counter and reference electrodes, respectively. The cathode and anode chambers were separated by a proton exchange membrane (PEM, Dupont, Nafion 117). The electrochemical NO_3^- reduction experiments were conducted using 16 cm^2 (exposed area 4 cm × 4 cm) working electrodes in the flow cells. During the operation, the electrolyte solution (0.5 M Na_2SO_4, pH: 7.0) was recirculated between the anode chamber and the anode tank, while the synthetic wastewater (15 mM NO_3^-, 10 mM Cl^-, 0.5 M Na_2SO_4, pH: 7.0) was recirculated between the cathode chamber and the wastewater tank. The water velocities in all chambers were 100 $mL\cdot min^{-1}$ to promote mixing and minimize the diffusion boundary layer.

2.3.2. Electrocatalytic reduction and recovery of NO3- toward (NH4)2SO4 (ERRNA)

On the basis of ERNA electrolysis cell, to realize simultaneous electrocatalytic reduction/recovery of NO_3^- to $(NH_4)_2SO_4$ (ERRNA), a tap chamber was added behind the cathode chamber. During the operation, the electrolyte solution (0.5 M Na_2SO_4, pH: 7.0) from anode chamber was recycled to the trap chamber. There is three chambers in the ERRNA electrolysis cell (Fig. 1(b) and S2): (i) anode chamber where the H^+ was produced, (ii) cathode chamber where NH_3 was synthesized, and (iii) trap chamber where H^+ was fed for the NH_3 capture. The Co-BTNA electrode was clipped to a flat sheet membrane (the nominal pore size 0.45 μm) composed of a polytetrafluoroethylene (PTFE) hydrophobic
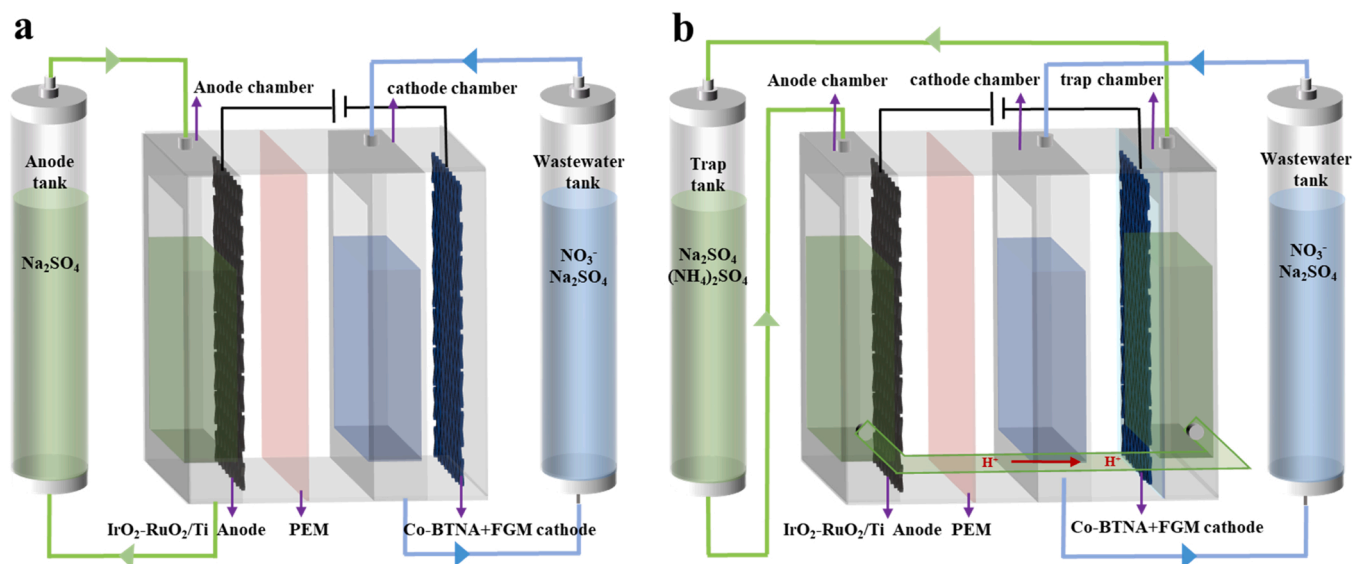
Fig. 1. The reactor configurations of the electrocatalytic NO_3^- reduction to NH_3 **(a)** and electrochemically upcycling NO_3^- into $(NH_4)_2SO_4$ **(b)**.

layer and a polypropylene (PP) substrate to construct a Co-BTNA composite cathode membrane assembly (reaction surface area: 4 cm × 4 cm). This composite membrane was inserted into the electrochemical flow cell. The PP substrate and the Co-BTNA electrode faced the trap and cathode chambers, respectively. The concentrations of NO_3^-, NO_2^- and NH_4^+ were determined by a UV–vis spectrophotometer as depicted in detail in the previous literature [27].

2.4. DFT calculation

Spin-polarized density functional theory (DFT) method was employed for all calculations using the Perdew-Burke-Ernzerhof functional as implemented in the Vienna Ab initio Simulation Package [28]. The exchange correlation functional under the generalized gradient approximation with projector augmented wave pseudo-potentials and the Perdew-Burke-Ernzerhof functional were adopted to describe the electron-electron interaction [29]. An energy cutoff of 450 eV was used and a K-point sampling set of 5 × 7 × 1 was tested to convergence. Force tolerance of 0.02 eV Å^{-1} and energy tolerance of 5.0×10^{-6} eV per atom were considered.

In reaction pathway calculations, the concept of computational hydrogen electrode was applied [30], so the chemical potential of the $H^+ + e^-$ was referenced by half of the chemical potential of H_2 at 0 V. The change of free energy of intermediates on the TNA, BTNA, Co-TNA and Co-BTNA surface was calculated based on Eq. (1).

$$\Delta G = G_{*A} - G_* - G_A \tag{1}$$

where G_{*A}, G_* and G_A denoted the total free energy of the adsorbed system, the clear surface and absorbates, respectively.

The Gibbs free energy was estimated under zero potential based on Eq. (2).

$$G = E + ZPE - TS \tag{2}$$

where E was the intermediate energy obtained from DFT calculations, ZPE was the zero point energy, T was the reaction temperature which was considered as 300 K here, and S denoted the entropy.

The quantum capacitance of TNA electrodes was defined as $C_Q = d_\sigma / d\phi_G$, where d_σ and $d\phi_G$ referred to the variations of charge density and local potential in TNA, respectively, and was given based on Eq. (3) [31]:

$$C_Q = e^2 \int_{-\infty}^{+\infty} D(E) F_T(E - \mu) dE \tag{3}$$

where $D(E)$ was the DOS, $F_T(E)$ was the thermal broadening function $[= (4kT)^{-1} \operatorname{sech}^2(E/2kT)]$, E was the relative energy with respect to E_F, μ was the chemical potential ($= e\phi_G$), and e was the elementary charge. σ was a function of ϕ_G and represented the cumulative excess charge in the electrode at a given electrode potential [32].

3. Results and discussion

3.1. Defect design and optimization for TNA catalysts

For electrocatalytic NO_3^- reduction to NH_3, the following criteria [33, 34] can be proposed for an eligible cathode catalyst: (1) the catalyst must possess good electrical conductivity to ensure high-efficiency electron transfer at the cathode-electrolyte interface; (2) the catalyst can facilitate the chemisorption of NO_3^- molecules to guarantee the sufficient activation of N-O bond; (3) the catalyst can stabilize *NO_2 and *NO intermediates to realize the high selectivity of NO_3^- to NH_3. All these desirable characters originate from the spatial and electronic structure of catalysts, and TiO_2 nanotube array (TNA) is promising to achieve the above three conditions via defect design [17,23]. As DFT calculations could gain deeper insights into the electrocatalytic mechanism and provide theoretical guidance for the experimental preparation of efficient TNA catalysts, systematical DFT investigations of the TNA catalysts modified with the Co heteroatom and OV defect were carried out to reveal their catalytic potential for NRA before actual experimental operation.

The rational creation and subtle modulation of lattice defects can well maneuver the conductivity from electronic properties. [21]. As shown in Fig. 2(a) and Fig. S3, the density of states (DOS) and band structures reveal the semiconductive character of TNA with an indirect band gap of around 2.4 eV, which is in line with previous studies and harmful to electron transport during electrocatalysis [17]. By introducing OV defects and Co heteroatoms on the surface, the band gaps of Co-TNA, BTNA and Co-BTNA are eliminated and Co-BTNA demonstrates the best conductivity among them due to the introduction of the occupied p and d orbitals of the OVs and Co atoms, suggesting its better intrinsic activity for NRA. The predominant peak of TiO_2 d states crosses the Fermi level also implying that the Co-BTNA catalyst had a higher carrier density. Fig. S4 gives a clearer picture of DOS near Fermi level,
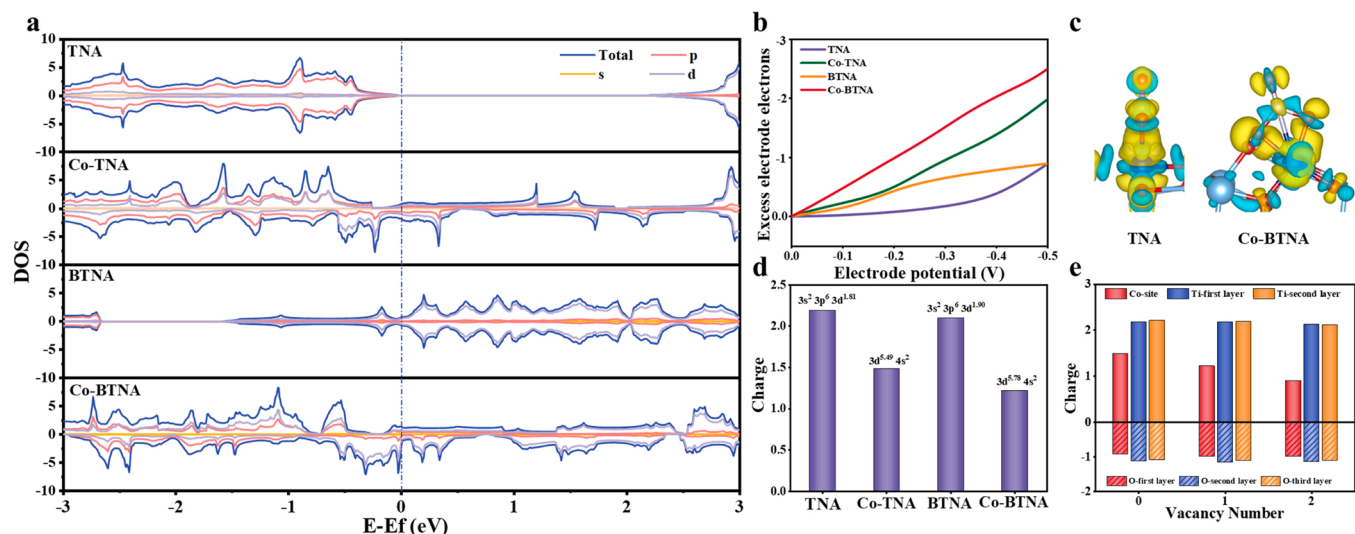
Fig. 2. Density of states diagrams of TNA, Co-TNA, BTNA and Co-BTNA (a). The total amount of excess electrons stored in the cathode of TNA, Co-TNA, BTNA and Co-BTNA under negative bias (b). The charge density distribution of *NO_3 on TNA (left) and Co-BTNA (right) (c). The charge of active sites on TNA, Co-TNA, BTNA and Co-BTNA (d). Comparison of atomic charges at different numbers of vacancies on Co-BTNA (e).

illustrating that coupling Co with OVs achieved the positive synergy effect on the conductivity of TiO_2, which was beneficial for the electrochemical NRA that relied on the electron transport between the electrode and the interface.

In addition to conductivity, the electron distribution at the interface is equally vital for catalysts to promote NO_3^- adsorption and electrochemical reduction. Following criterion 2, the cumulative excess charge in the cathode at a given potential was investigated. Fig. 2(b) clearly shows that the Co-BTNA electrode generally stored more electrons than pristine or single doped TNA within the − 0.5 V window. The increased charge capacity (Fig. S5) means a lower potential was required for the Co-BTNA electrode to achieve the same charge density [32]. Considering the spontaneous electron transfer from the active site to the adsorbate during NO_3^- adsorption (Fig. 2(c) and Table S3), Co-BTNA was conducive to the NO_3^- adsorption at the electronic level. Charge analysis of different active sites was also applied to verify the ease of electron transfer during NO_3^- reduction after adsorption (Fig. 2(d)). Relative to

the paired electrons, the unpaired electrons on 3d orbital of all active sites were more easily induced by the nitrogen and oxygen of NO_3^- with larger electronegativity due to their poor stability, and then participated in the subsequent hydrodeoxygenation. Thus, Co-based active centers were expected to have better performance because the highly occupied d orbitals ($d^{5.78}$ and $d^{5.49}$) of Co atoms were more prone to loss electrons to achieve a stable half-filled electron configuration. The role of OVs was also elucidated by comparing the charge of active sites with different OV contents on Co-BTNA. As shown in Fig. 2(e) and Fig. S6, the net charge of Co site reduced with the increase of the OVs content, indicating that more electrons gathered at the active site, which was beneficial to the charge transfer from active site to NO_3^- and accelerated the latter's adsorption and reduction. Given that above, it can be concluded that the doped Co and OV defects could effectively improve the conductivity and electron transfer of TNA, which facilitated the reaction activity of NO_3^-.

Besides the activity, the selectivity of NH_3 was further investigated to predict the real NRA performance of different TNA cathodes according
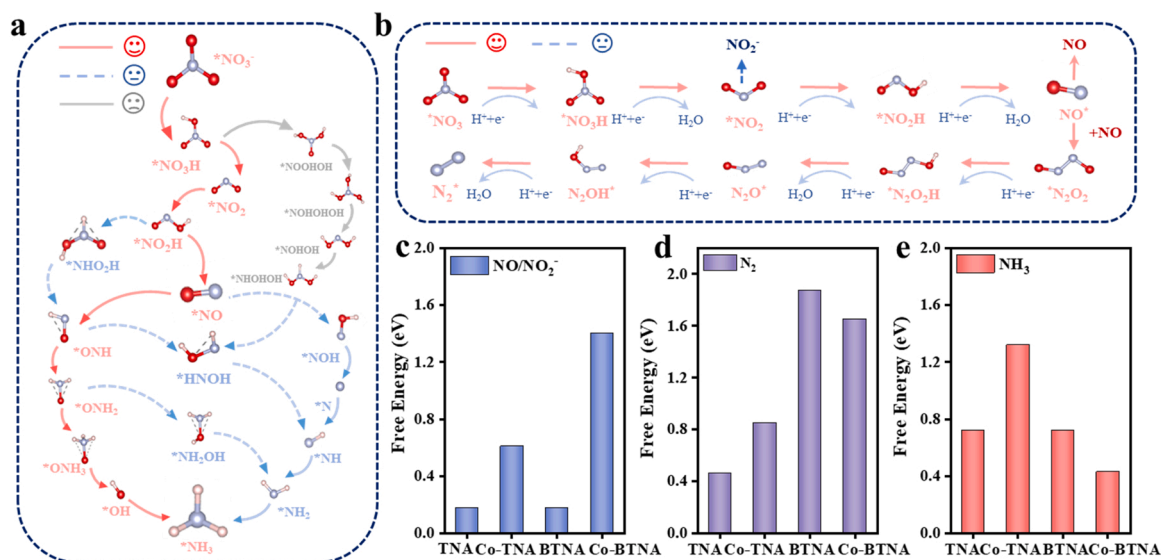

Fig. 3. Schematic diagram of possible reaction pathways for NO_3^- electroreduction to NH_3 on the Co-BTNA (a). Schematic diagram of possible reaction pathways for NO_3^- electroreduction to N_2 on the Co-BTNA (b). The energy barriers of NO_2/NO (c), N_2 (d), and NH_3 (e) production on the surface of TNA, BTNA, Co-TNA and Co-BTNA.

to criterion 3. A variety of by-products, namely, N_2, NO_2^- and NO were likely to form in the electroreduction from NO_3^- to NH_3. Thus, to clarify what happened during the process of NRA, the comprehensive electrocatalytic reduction pathways on TNA, Co-TNA, BTNA and Co-BTNA were outlined in Fig. 3(a) and (b) based on the intermediates identified in previous studies [35]. The specific calculated free energy of reaction intermediates that shown in Fig. 3(a) and (b) on TNA, BTNA, Co-TNA and Co-BTNA for NO_3^- electroreduction to NH_3/N_2 were listed in Table S2 and Table S3. On different catalysts (Fig. 3(a) and S7), two possible NH_3 generation pathways were canvassed regarding different adsorption structures of NO (O-end, N-end) as demarcation [34]: one was the NOH pathway from *NO to *NOH (*NOH → *N → *NH → *NH$_2$ → *NH$_3$) and the other was the ONH pathway from *NO to *ONH (*ONH → *ONH$_2$ → *ONH$_3$ → *OH→*). The latter was found on most TNA catalysts as the red line plotted in Fig. 3(a) and Fig. S7, while single Co doping offered the potential to change the pathway. Fig. 3(b) and Fig. S8 show the same generation pathways for by-products on different catalysts, illustrating that the part of *NO and *NO$_2$ intermediates were desorbed from the surface to produce NO and NO_2, and N_2 was produced after *N$_2$O$_2$ and *N$_2$O generation by association of free by-products' with *N or *NO.

The free-energy diagram in Fig. 3(c) shows that the energy barriers for the release of NO_2/NO were 0.18 eV on TNA, 0.61 eV on Co-TNA, 0.18 eV on BTNA and 1.4 eV on Co-BTNA, respectively, implying that the doped Co atoms inhibited the desorption of *NO and *NO$_2$ and then reduced the formation of all by-products by modifying the number of key intermediates. Meanwhile, Fig. 3(d) and (e) demonstrates that high energy barriers for the formation of N_2 were needed on BTNA (1.87 eV) and Co-BTNA (1.65 eV) compared with TNA (0.46 eV) and Co-TNA (0.85 eV), versa, the energy barriers for the formation of NH_3 were decreased from 1.32 eV on Co-TNA to 0.43 eV on Co-BTNA, suggesting that OV defects in TNA catalysts could increase the formation barrier of N_2 and boosted the production of NH_3. In summary, our theoretical studies confirmed the optimization of TNA catalytic performance derived from the synergistic effect between Co and OVs, and validated that Co-BTNA can be used as a promising fast, low-energy electrocatalyst for NRA with high activity and selectivity.

3.2. Physicochemical and electrochemical characterizations

3.2.1. Physicochemical characterizations

Encouraged by the DFT calculation results, the Co-BTNA electrocatalyst with theoretically excellent NRA performance was experimentally prepared on the Ti mesh by simple anodization and drop-casting methods. From SEM images (Fig. 4(a) and Fig. S9), it is clearly observed that the TNA and Co-BTNA layer were compact, ordered arrays of nanotubes with the average diameter of around 80 nm, and the large porosity was highly favorable for uniform doping of Co atoms. The representative TEM and EDS mapping images of Co-BTNA are shown in Fig. 4(b)-(f)), revealing that O, Ti and Co elements were distributed homogeneously. No particulate cobalt oxide could be found, indicating that all Co atoms were immobilized on the tube wall of Co-BTNA [13]. The doping amount of Co in Co-BTNA was about 0.17 μmol/cm^2 as detected by the inductively coupled plasma atomic emission spectrometry, which was line with the previous study [20]. Except the diffraction peaks at $2\theta = 38.42°$, $40.17°$, $53.00°$, $62.94°$, $70.66°$ and $76.22°$ identified as Ti, Fig. 4(g) shows that the similar XRD patterns of TNA and Co-BTNA with diffraction peaks at $2\theta = 25.3°$, $48.03°$, $53.88°$ and $62.68°$ were identified as the pure anatase phase of TiO_2 with the preferential exposure of (101) plane, indicating that the doping of Co did not induce any phase transition [13,36]. By magnifying the diffraction information of TNA and Co-BTNA in Fig. S10, it was found that the diffraction intensity of (101) plane was decreased after Co doping [20], which was ascribed to the different ionic radius between Co^{2+} (0.65 Å) and Ti^{4+} (0.61 Å) and thus indicated Co doping in the TiO_2 lattice [37].

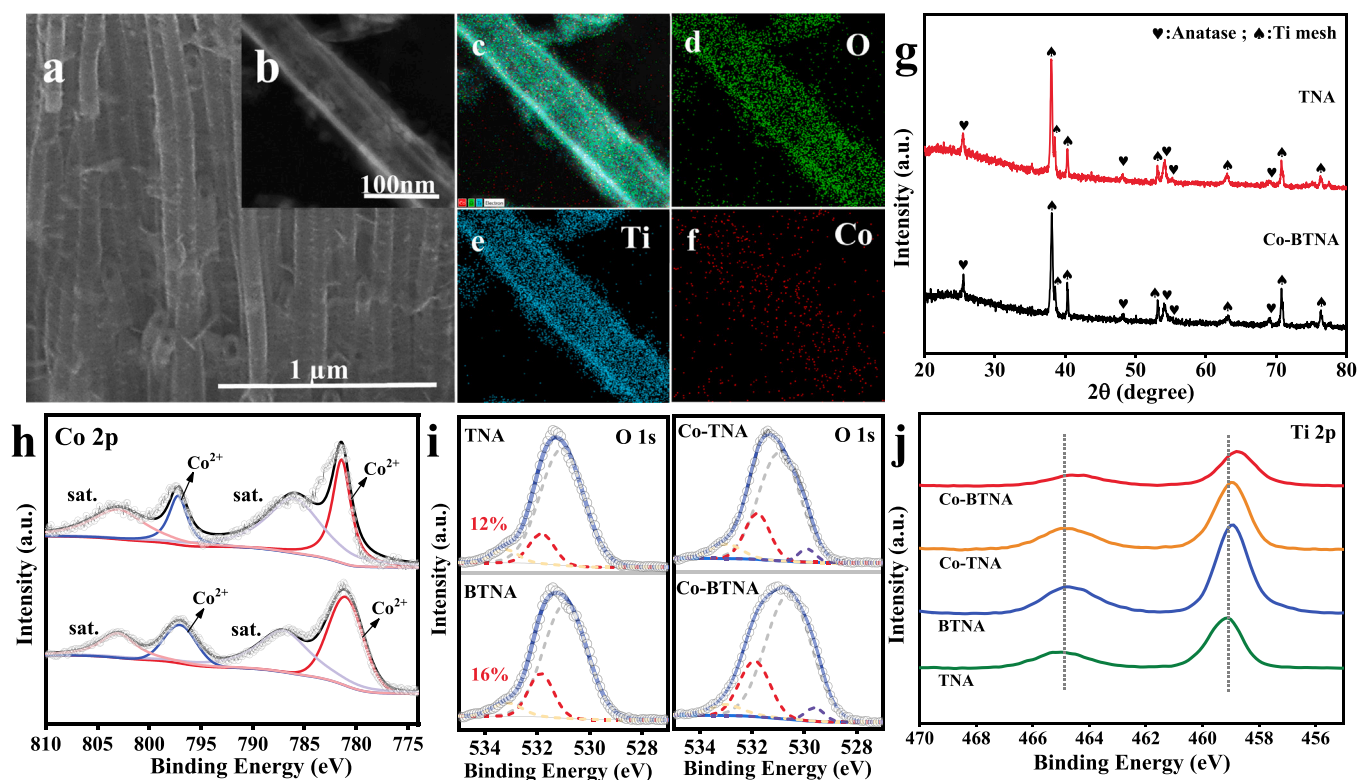Oxidation states and OVs were further analyzed by XPS spectra. As

Fig. 4. SEM cross-section image of Co-BTNA electrode (a). TEM image of the Co-BTNA (b). The elemental mapping images of Co-BTNA (c)-(f). XRD patterns of TNA and Co-BTNA (g). XPS spectra of Co 2p signals in Co-BTNA and Co-TNA (h). O 1 s signals in bare TNA, BTNA, Co-TNA and Co-BTNA (i). Ti 2p signals in Co-BTNA, Co-TNA, BTNA, and bare TNA (j).

shown in Fig. 4(h), the two fitted peaks of Co 2p3/2 and 2p1/2 at 781 eV and 797 eV were assigned to Co^{2+} [38] and they were shifted to a higher binding energy compared to the spectra of Co_3O_4 (of which Co 2p3/2 orbital located at 780, indicating the mixed +3/+2 states.) [39]. Given that no CoO_x particulates could be found by both SEM and TEM, and Co species on Co-BTNA still remained in Co^{2+} after electroreduction. It can be concluded that Co^{2+} is atomically doped into the lattice of TiO_2 and its reduced valence state does not result from electroreduction but from a strong $Co-TiO_2$ interaction [13]. Electrochemical reduction promotes the formation of Ti^{3+} and OVs on TNA [13,15]. As shown in Fig. 4(i), for TNA and BTNA, the O 1s XPS spectra were deconvoluted with three major peaks. The peaks centered at 530–531 eV and 532–533 eV were assign to the lattice oxygen and hydroxyl group, respectively [40]. The peak located at 531.8 eV was assigned to the adsorbed oxygen (O_2^{2-} or O^-), which was originated from the dissociative adsorption of molecular oxygen on the surficial OVs and could serve as an indirect measurement of native OVs. [13,41]. By peak deconvolution, it was found that BTNA had the higher relative concentration of adsorbed oxygen (18 %) compared with bare TNA (12 %), indicating that the formation of OVs can be effectively promoted by electrochemical reduction. However, it is difficult to quantitatively analyze the OVs concentration for Co-TNA and Co-BTNA, because the peak of O 1s of oxidized Co (hydroxyl group, 531.7 eV) was coincided with that of O 1 s of TiO_2 (adsorbed oxygen, 531.7 eV), and the peak of O 1s of oxidized Co (adsorbed oxygen, 530.9 eV) was coincided with that of O 1s of TiO_2 (lattice oxygen, 530–531 eV) [23,42], as shown as red line and gray line of Co-TNA and Co-BTNA in Fig. 4(i). Considering that there was just trace amount of Co doping into TiO_2 and the formation of OVs was together with a partial reduction of Ti^{4+} to Ti^{3+} during electrochemical reduction, the concentration of OVs can be qualitatively measured by Ti^{3+} [14]. Similar method has also been used in other literatures that focus on trace amount of heteroatom doping in TiO_2 nanotube [13,20].

As shown in Fig. 4(j), the Ti $2p_{3/2}$ and Ti $2p_{1/2}$ peaks at 458.9 eV and 464.7 eV can be assign to Ti^{4+} of TNA [43]. Whereas, for BTNA, Co-TNA and Co-BTNA, they were shifted to a lower binding energy compared with TNA because electrochemical reduction and doping of Co induce a partial reduction of Ti^{4+} to Ti^{3+} together with the formation of OV defects. For BTNA, the cathodization rendered insignificant change in Ti state (0.17 eV) probably due to a large fraction of surficial Ti^{3+} sites that can be readily oxidized in ambient air. As compared with BTNA, the binding energy shift for Co-BTNA (0.35 eV) from TNA was clear, indicating that the Ti^{3+} (OVs) formation is more favorable when the neighboring Ti is substituted by Co, because Co forms a weaker bond with O in comparison to Ti, as reflected in the formation energy of TiO_2 (-3.5 eV atom^{-1}) in comparison to the Co oxides (Co_3O_4, -1.4 eV atom^{-1}; CoO, -1.3 eV atom^{-1}; CoO_2, -1.1 eV atom^{-1}) [44]. These results indicated that Co doping facilitates the formation and stabilization

of Ti^{3+} (OVs). Besides, since the formation of OVs reduced the coordination of the metal ions, the apparent oxidation states should be lower than those sites in the pristine material, which was in line with the reduced Ti and Co valence states in Co-BTNA.

3.2.2. Electrochemical characterizations

The real electrocatalytic reduction ability of the as-prepared Co-BTNA was tested to verify the thermodynamic changes brought about by the synergistic Co doping together with OV defects on TNA. Electrochemical impedance spectroscopy (EIS) was used to evaluate the charge transfer resistances of different TNA electrodes. Since the smaller arc size in EIS Nyquist plot correlates to the smaller charge transfer resistance on the electrode surface[45], the descending order of arc size (TNA > BTNA > Co-TNA > Co-BTNA) in Fig. 5(a) suggested that the electron transfer in the Co-BTNA was more efficient than other TNA electrodes, implying that the doped Co and OV s triggered a notable improvement on the conductivity of TNA, which was consistent with the analysis in Section 3.1. The linear sweep voltammetry (LSV) tests of the Co-BTNA and two control samples, Ti and BTNA, were then performed under various electrolytes to determine the origin of catalyst activity. As shown in Fig. 5(b), a more prominent reduction current was observed during nitrate reduction on Co-BTNA, which was dramatically improved from that of either Ti and BTNA, and the Co-BTNA cathode also had the most positive onset potential of -0.82 V/SCE for electrocatalytic reduction of NO_3^- in comparison with BTNA cathode (-1.25 V/SCE) and pure Ti cathode (-1.68 V/SCE), indicating the high activity of NRA on the doped Co sites. Compared with the system without nitrate, the current density of Co-BTNA with nitrate was enhanced, suggesting the occurrence of nitrate electroreduction (Fig. S11). In addition, the potential of NO_3^- reduction was higher than that of H_2 evolution reaction (HER) (-1.36 V/SCE) at the Co-BTNA cathode, and no obvious substantial HER was observed when more negative potentials were applied, indicating the poor HER activity of Co-BTNA over a wide range of negative potentials. (Fig. S11c) The preferential occurrence of NO_3^- electroreduction could help improve the selectivity for NH_3 synthesis. Note that the onset potential was consistently defined as the potential under which -5 mA·cm^{-2} was reached in LSV for NRA and HER in this work.

As nanotube structure endowed Co-BNTA with abundant active sites, to exclude the effect of active area and compare the intrinsic activity of the catalyst, electrochemical double-layer capacitance (C_{dl}) tests were performed to normalize the current density over the electrochemical active surface area (ECSA) (Fig. S12). Different slopes from these linear fits determined the C_{dl} of Co-BTNA, BTNA and Ti to be 0.359 mF·cm^{-2}, 0.253 mF·cm^{-2} and 0.115 mF·cm^{-2}, respectively (Fig. 5(c)). But ECSA-normalized I-V curve illustrates Co-BNTA still showed the best intrinsic activity for NRA (Fig. S11). These results clearly demonstrated
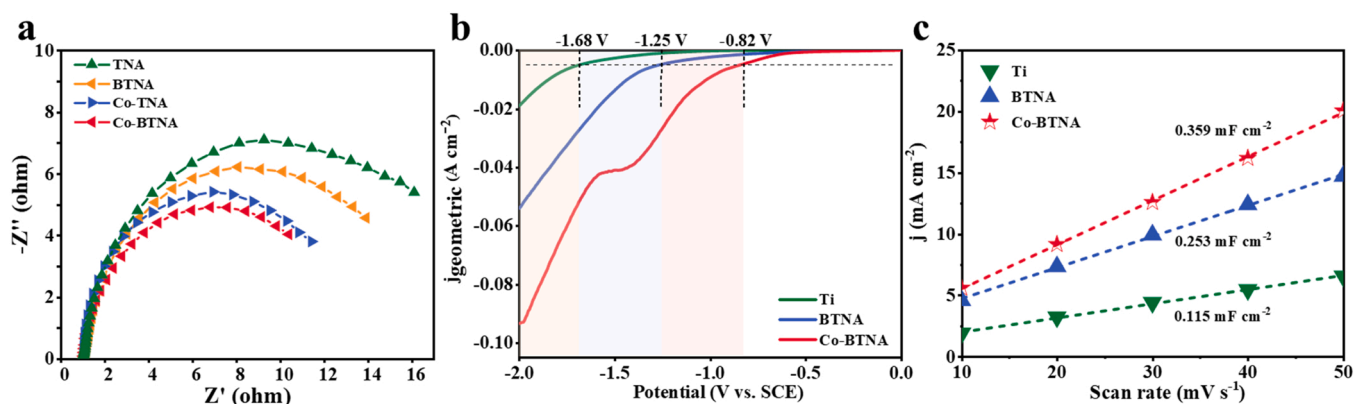

Fig. 5. Nyquist plots of Co-BTNA, Co-TNA, BTNA, and TNA (a). LSV curves of Ti, BTNA and Co-BTNA during NO_3^- reduction (b). Calculation of double capacitance for Ti, BTNA and Co-BTNA cathodes based on the 1 cm^{-2} electrode geometric surface area (c).

that the good performance of Co-BTNA originated not only from the high surface area, but also from the excellent intrinsic activity.

3.3. Electrocatalytic performances

3.3.1. Outstanding electrocatalytic NO_3^- reduction performance of Co-BNTA

The electrocatalytic NRA activity of Co-BTNA was then investigated in the ERNA reactor. According to Fig. 6(a), the NO_3^- conversion and selectivity toward NH_3 on pure Ti were only 18 % and 31 %, indicating the negligible activity and insignificant contribution of Ti substrates to NRA. Compared with the unremarkable NO_3^- removal rate (77 %) and NH_3 selectivity (76 %) of BTNA, Co-BTNA showed a more prominent reduction current with the NO_3^- conversion and NH_3 selectivity of 96 % and 91 %, and the pseudo-first-order kinetic constants (k_{ap}) of Co-BTNA was 0.02662 min^{-1}, which was 1.86 times and 20.79 times higher than those of BTNA (0.01435 min^{-1}) and Ti (0.00128 min^{-1}), respectively (Fig. 6(b)), which suggested facile kinetics and high activity of NRA on the doped Co sites. All NH_3 was produced by the reduction of NO_3^- (Fig. 6 (c)) and almost no NO_2^- was produced on Co-BTNA during the whole process (Fig. S13). Only 0.45 % of Co in the Co-BTNA electrode was lost (which was 0.0586 $mg·L^{-1}$, much lower than the discharge standard in industrial wastewater (1 $mg·L^{-1}$) based on GB/T 25467–2010 of China [46]), indicating that Co-BTNA exhibited high stability and activity toward NO_3^- to NH_3.

The working potential could greatly influence the reduction performance during electrochemical process, so the effects of various applied potentials on the Faradic efficiency (FE) and selectivity for the NH_3 were studied for Co-BNTA. As shown in Fig. 6(d) and S14, from − 1.6 V to − 2.4 V, the conversion rate of NO_3^- gradually increased from 80 % to 97 % and there was no obvious difference in the NH_3 selectivity, indicating that it possessed excellent activity for NH_3 production over a wide range of operating potential. The Faradaic efficiency for the first 20 min (FE_{20}) displayed a volcanic shape curve with a maximum of 82.5 % at − 1.8 V,

while the Faradaic efficiency for the whole reaction time (FE_{120}) were decreased monotonically from 43 % to 12 % with working potential increasing from − 1.6 V to − 2.4 V. This phenomenon was mainly caused by the fact that competitive HER was inhibited by high NO_3^- concentration at the beginning of reduction but intensified with the decreasing of the remaining NO_3^-. Most of electrical energy was wasted for H_2O electrolysis and H_2 production at high working potential, therefore, a gradually reduced three-stage potential operation was used to balance NO_3^- removal efficiency and energy consumption. As shown in Fig. 6(e), compared with the − 2.4 V potentiostatic operation, the three-stage potential operation had seldom effect on the conversion and selectivity, which were 95.6 % and 90.95 %, respectively. Interestingly, the FE_{120} increased from 11.19 % to 39.5 %, and energy consumption decreased from 95.0862 $kWh·Kg^{-1}N$ to 64.06 $KWh·Kg^{-1}$ N (Fig. S15). Given that, three-stage potential operation was used in our further work.

Cl^- in wastewater also affected the selectivity of NH_3 when there was no proton exchange membrane (PEM) between cathode and anode, as Cl^- could be oxidized on the anode to form Cl_2 which then reacted with water to give ClO^- that effectively oxidized NH_4^+ to N_2 [24]. Fig. 6(f) shows all the NH_4^+-N selectivity, NH_3 yield rate, and partial current density toward NH_3 production (j_{NH3}) decreased significantly when the Cl^- concentration increased from 10 mM to 50 mM in the feed tank without PEM. By contrast, when the PEM was inserted between cathode and anode, the N_2 formation on anode was largely prevented as PEM did not permit the transfer of NH_4^+ and ClO^-, which resulted in the increase in NH_4^+-N selectivity, NH_3 yield rate, and j_{NH3} from 29.4%, 0.019 $mmol·h^{-1}·cm^{-2}$, and 2.0 $mA·cm^{-2}$ to 91%, 0.048 $mmol·h^{-1}·cm^{-2}$, and 9.39 $mA·cm^{-2}$, respectively, at 10 mM Cl^-.

3.3.2. Self-optimization of catalytic performance in electrocatalysis

During the experiment, the Co-BNTA cathode showed an interesting phenomenon that the selectivity toward NH_3 increased from 88.6 % to 93.2 % after two hours of reaction, while the NO_3^- removal rate was slightly improved (Fig. 7(a)). It could be speculated that the self-
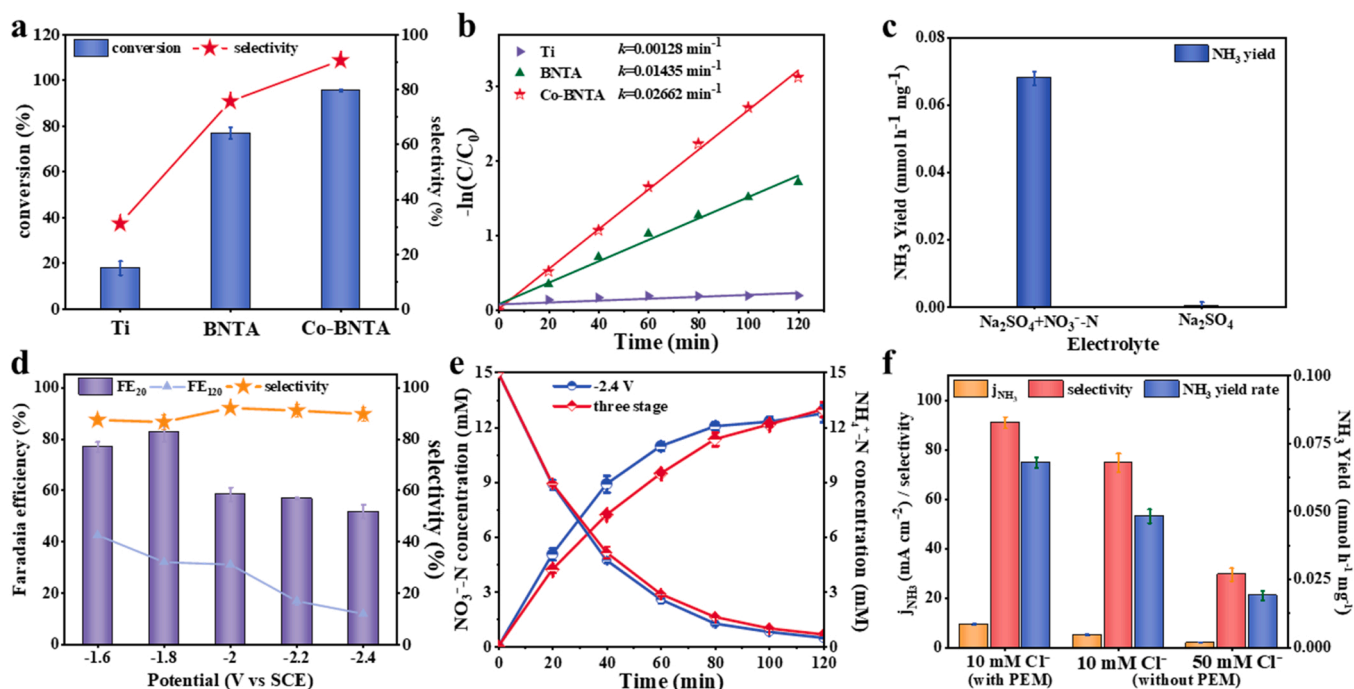

Fig. 6. Comparison of selectivity and NO_3^- conversion rate on Ti, BTNA and Co-BTNA (a). The linearized pseudo first-order kinetic profiles of Ti, BTNA and Co-BTNA (b). Ammonium yield rate over Co-BTNA in Na_2SO_4 electrolyte with and without NO_3^- (c). Faradaic efficiency and selectivity of NH_4^+ over Co-BTNA at given potentials (d). Time-dependent concentration of NO_3^- and NH_4^+ over Co-BTNA at given potentials (Three-stage potential operation: −2.4 V (20 min); − 2 V (40 min); − 1.6 V (60 min)) (e). The selectivity, NH_3 yield rate, and partial current density toward NH_3 production (j_{NH3}) at different Cl^- concentrations with/without PEM between anode and cathode (f). (Experimental conditions: initial NO_3^- concentration: 15 mM, pH: 7.0, Cl^-: 10 mM).
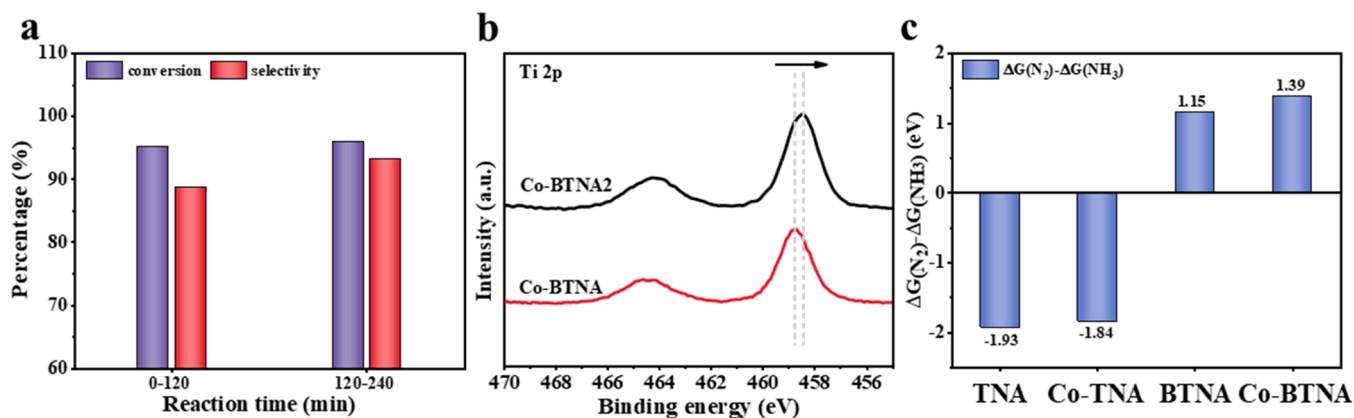
Fig. 7. Comparison of NH$_3$ selectivity and NO$_3$ conversion rate at different reaction time **(a)**. XPS spectra of Ti 2p signals of Co-BTNA2 (the Co-BTNA after 2 h reaction) **(b)**. Free energy difference between NH$_3$ and N$_2$ pathway **(c)**.

optimization of catalytic performance originated from the change in the number of Ti^{3+}(OVs) in the Co-BNTA electrode, because the XPS results in Figs. 4(j) and 7(b) clearly showed that the Ti 2p of Co-BTNA used for two hours (Co-BTNA2) was shifted to a lower binding energy compared with the unused Co-BTNA, which indicates that the OVs concentration will further increase after two hours of reaction. Considering Co-BTNA as cathodes, the variation of OVs concentration was derived from the cathode bias in the first two hours. Section 3.1 have proved that the addition of OVs facilitated the removal of NO$_3$ by promoting electron accumulation at the active site (Fig. 2(e)) and inhibited the formation of N$_2$ by-products by raising the energy barrier (Fig. 3(d)). Fig. 7(c) shows the competitive generation between NH$_3$ and N$_2$ pathway intuitively. As the larger in difference meant the more difficult to produce N$_2$, the free energy difference of − 1.93 eV and − 1.84 eV for TNA and Co-TNA

implied the easy generation of N$_2$, while the values as high as 1.15 eV and 1.39 eV for BTNA and Co-BTNA illustrated that the increase in the number of OVs significantly improved the selectivity of NH$_3$. Thus, it can be deduced that cathode bias could induce the increase of OV concentration, which promoted the NO$_3$ reduction and suppressed the by-product production [17], leading to the self-optimization of catalytic performance for Co-BTNA in NRA.

3.4. Practical application of Co-BTNA for NO$_3$ upcycling towards (NH$_4$)$_2$SO$_4$ from synthetic wastewater

With the impressive NRA performance of Co-BTNA catalyst, we further demonstrated its practical applications in an ERRNA electrolysis cell to continuously collect high-purity ammonia products ((NH$_4$)$_2$SO$_4$).
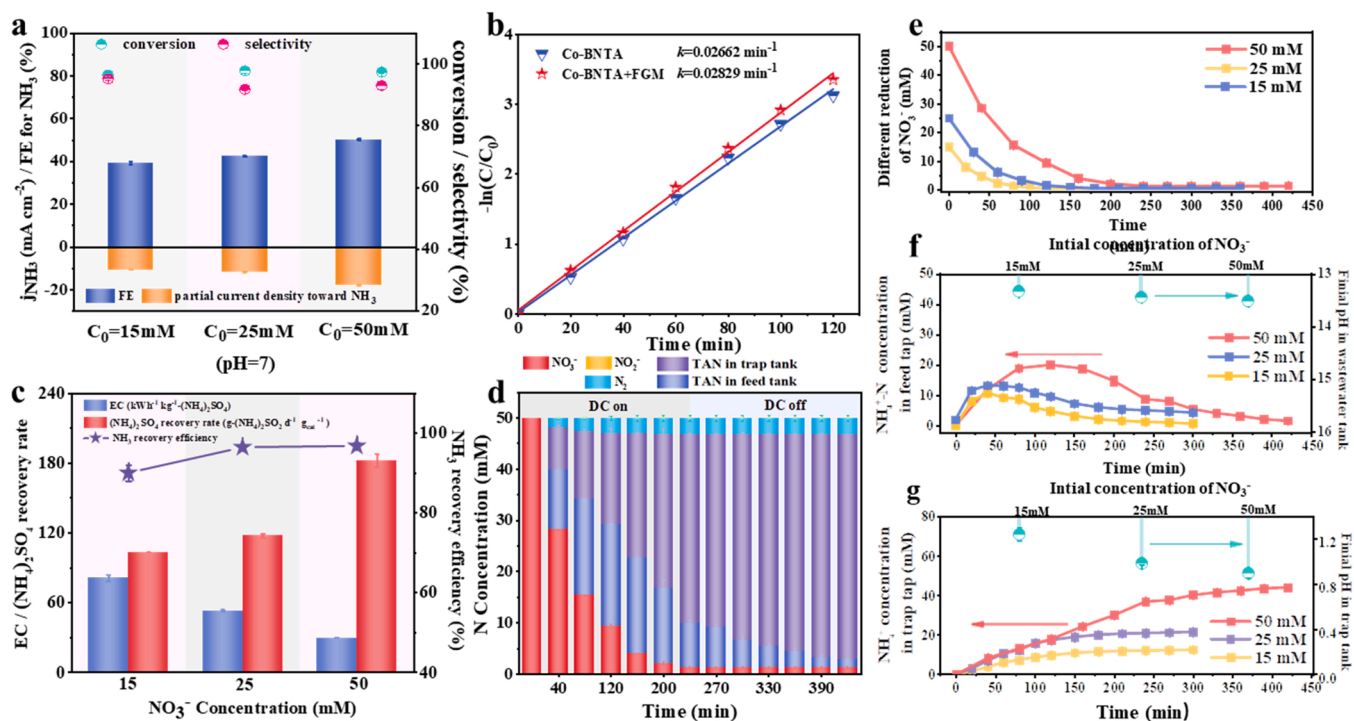

Fig. 8. Faradic efficiency, partial current density towards NH$_4^+$, NO$_3$ conversion and NH$_4^+$ selectivity at different feed NO$_3$ concentrations (a). The comparison of the linearized pseudo first-order kinetic with and without FGM and acid circulation (b). Energy consumption, (NH$_4$)$_2$SO$_4$ recovery rate and NH$_3$ recovery efficiency at different feed NO$_3$ concentrations (c). The concentration evolution trends of various N species (d). Difference in NO$_3^-$ reduction at various NO$_3$ concentrations (e). NH$_4^+$ amounts and finial pH in wastewater tank (f) and trap tank (g) at various NO$_3$ concentrations. All data obtained in the ERRNA device with Co-BTNA as cathode. (Specific testing conditions: cathode, Co-BTNA; FGM, 0.45 μm; pH: 7.0, reaction time, 3.0–5.0 h; applied potentials (three stage operation), NO$_3$ concentrations, are shown in the figure.).

The localized high pH (12−14) on the cathode surface drove the conversion of NH_4^+ to NH_3 that could be readily volatilized and harvested through the flat-sheet gas membrane (FGM) placed at the back of the cathode [47]. Meanwhile, The solution pH of the anode chamber could rapidly drop below 2.0 in the current density range of 10–50 mA cm^{-2} when the electrolyte is neutral [48]. After recycling to trap chamber, under this low pH environment, nearly 100 % of the stripped NH_3 could be stably maintained as $(NH_4)_2SO_4$ [49]. Furthermore, due to the electrostatic repulsion and low catalytic activity of IrO_2-RuO_2/Ti anode for NH_4^+ [50], the direct oxidation of ammonia species was avoided as their interaction with the anode was negligible [51].

Since different NO_3^- sources have a wide range of NO_3^- concentrations, continuous-flow experiments over a range of initial NO_3^- concentration were evaluated to demonstrate the broad adaptability of Co-BTNA cathodes in ERRNA. Fig. 8(a) shows that nearly 100 % NO_3^- was removed at different initial concentrations, of which approximately 91.8–95.2% could be converted to NH_4^+. The FE for the whole reaction period and partial current density towards NH_4^+ were increased to 50 % and − 18.0 mA·cm^{-2} when increasing NO_3^- concentration from 15 mM to 50 mM (Fig. 8(a)). Notably, compared with the Co-BTNA in ERNA device (91 %, 0.02662 min^{-1}), the selectivity and pseudo-first-order kinetic constants of Co-BTNA in collaboration with the ENNRA device were up to 95.2 % and 0.02829 min^{-1} (Fig. 8(b)), primarily because of the addition of the acid cycling and gas permeable membrane that enhanced the transport of gaseous NH_3 to the trap chamber and reduced the blocking effect on the active sites of Co-BTNA cathode, which in turn increased the activity and NH_3 selectivity of NRA [47].

The corresponding NH_3 recovery process was then investigated. Fig. 8(c) clearly shows that with initial NO_3^- concentration increasing from 15 mM to 50 mM, the NH_3 recovery efficiency and $(NH_4)_2SO_4$ recovery rate increased from 90 % to 96.7 % and 103.44–182.25 g-$(NH_4)_2SO_4 \cdot d^{-1} \cdot g_{cat}^{-1}$, respectively, which were attributed to the mass transfer limitation of NO_3^- and subsequent $(NH_4)_2SO_4$ generation [25]. Accordingly, both the energy consumption (EC) with/without the energy cost of catalyst preparation decreased from 71.9 to 27.1 kWh·kg$^{-1}(NH_4)_2SO_4$ and from 83.90 to 30.68 kWh·kg$^{-1}(NH_4)_2SO_4$, which outperformed the most of the reported studies for physicochemical electrochemical treatment of NH_3 recovery to date (Fig. 8(d), Fig. S17 and Table S4). These results suggest that saline wastewaters with high-strength NO_3^- are preferred for electrochemical upcycling of NO_3^- into $(NH_4)_2SO_4$. However, for normal wastewater streams that have fairly low nitrate concentrations, one approach that combines the ERRNA system with concentration processes such as reverse osmosis and ion exchange appears feasible. For example, the unmanageable waste brines from these two processes with high NO_3^- concentrations (>1000 mg L^{-1}) are ideal media for the ERRNA system.

For the system with the initial NO_3^- concentration of 50 mM, the detailed concentration changes of the different N-species in Fig. 8(e)-(g) reveals that nearly 100 % NO_3^- from the feed stream was effectively transferred into NH_3/NH_4^+ within 240 min of operation, during which 80.9 % of the produced NH_3 (36.8 ± 0.18 mM) was recovered into the trap chamber as $(NH_4)_2SO_4$, and the residual NO_3^-, NO_2^- and NH_4^+ in the cathode chamber were 1.29 ± 0.027, 0.034 ± 0.033 and 8.67 ± 0.6 mM respectively. Longer hydraulic retention time have been demonstrated to achieve extra 15.8 % recovery rate by increasing the diffusion time of NH_3 (g) across the FGM [52], while the DC power was turned off after 240 min to reduce EC because almost all the remaining NH_4^+ existed in the form of dissolved NH_3 (aq) due to the high electrolyte pH (13.5 ± 0.080) in the cathode chamber, and the remaining H$^+$ (pH: 0.90 ± 0.043) in trap and anode chambers was sufficient to protonate the remaining NH_3 in the feed tank (100 mL) [53]. Overall, a sharp increase in the amount of NH_3/NH_4^+ in feed tap was observed in the first two hour, and then the value gradually reduced and reached a relatively stable concentration, while the amount of NH_4^+ in trap tap was gradually increased (Fig. 8(e)-(g)). Similar trends were observed upon operation under different initial NO_3^- concentration, suggesting that the strategy for direct conversion of NO_3^- containing influent into ammonia products $((NH_4)_2SO_4)$ using Co-BTNA cathode and ENNRA unit is efficient and broadly applicable.

3.5. The NO3- removal and NH3 generation mechanism

To gain deeper insight into the enhanced catalytic performance of Co-BTNA for NRA, the reaction mechanism was elaborated from two different pathways, namely electron transfer reduction and atomic hydrogen (·H) reduction [24]. As the former relies on the direct electron transport between the adsorbate and the electrode, the minimum energy pathway of NRA was calculated for different catalysts using the DFT method. Fig. 9(a) clearly shows that the high energy barriers for the formation of by-products (NO, NO_2 and N_2) and low energy barrier for NH_3 formation were needed on Co-BTNA when the pathway branched (steps marked by shadows), which was the main reason why Co-BTNA boosted the yield and selectivity of NH_3 compared with TNA, BTNA and Co-TNA. The poorer performances of TNA and Co-TNA were attributed to the weak adsorption of NO_3^- (−0.45 eV and −0.94 eV), which implied that the catalysts had poor ability to stabilize reactants in the fluid field, resulting in easy generation of dinitrogen by linking free by-products. OV defects increased the NRA reactivity and selectivity to NH_3 by reducing NO_3^- adsorption energy to − 4.58 eV and − 2.49 eV for BTNA and Co-BTNA, but the accompanying energy gap of *OH + H$^+$ + e$^-$ → * + H_2O on BTNA (4.42 eV) indicated that the OVs in BTNA were difficult to be recovered without Co doping. Therefore, the moderate adsorption of reactants arising from the synergistic effect between Co and OVs played a key role in the direct electron transfer reduction of NRA.

Moreover, the·H produced by catalyst can also promote the high catalytic activity of Co-BNTA via favoring the chemical reduction of free NO_3^-, as Fig. S16 shows that the formation energy of·H on the Co-BTNA (0.419 eV) is much smaller than that on TNA (2.68 eV), TNA (0.8 eV) and BTNA (0.75 eV). To verify the existence of ·H, the radical quenching experiment with the tert-butyl alcohol (TBA) as quenching agent was conducted to evaluate the contribution of ·H to the reduction of NO_3^- on the Co-BTNA cathode. As shown in Fig. 9(b) and (c), the NO_3^- residual gradually increased with the concentration increase of TBA. After the addition of TBA to quench ·H, the linearized pseudo first-order kinetic profiles of Co-BTNA dramatically decreased from 0.02662 to 0.01676, indicating that the ·H reduction contributed nearly 37 % to the removal rate of NO_3^-, which might be the reason why the selectivity of NH_3 on Co-BTNA cannot reach 100%. The two different reduction pathways explained why Co-BTNA had a superior performance for NH_3 production via NRA compared to TNA, Co-TNA and BTNA, and highlighted the importance of modifying TNA with the Co heteroatom and OV defect.

4. Conclusion

In summary, guided by the defect engineering results in DFT, a high-performance NRA catalyst (Co-BTNA) was successfully designed and prepared by modifying TiO_2 nanotube cathode with the Co heteroatom and OV defect simultaneously. The raised electrical conductivity and surface charge density due to defect engineering facilitated the activity toward NO_3^-, while the OV defects increased the formation barrier of N_2 and the doped Co suppressed the desorption of *NO/*NO_2, thereby boosting the production of NH_3 at a low energy barrier (0.43 eV). Practical experiments showed that the Co-BNTA catalyst maintained a high NH_3 selectivity of 91% and an excellent FE of 85% when the initial NO_3^- concentrations was 15 mM. By coupling the Co-BTNA electrocatalyst with an ERRNA device, the NH_3 produced by NO_3^- reduction at the cathode was vaporized directly through the FGM and recovered as $(NH_4)_2SO_4$ by the acid produced at the anode, which achieving 100% of NO_3^- conversion and 96.7% of NH_3 recovery, delivering 182.25 g-$(NH_4)_2SO_4 \cdot d^{-1} \cdot g_{cat}^{-1}$ of N-fertilizer recovery rate at an energy demand of
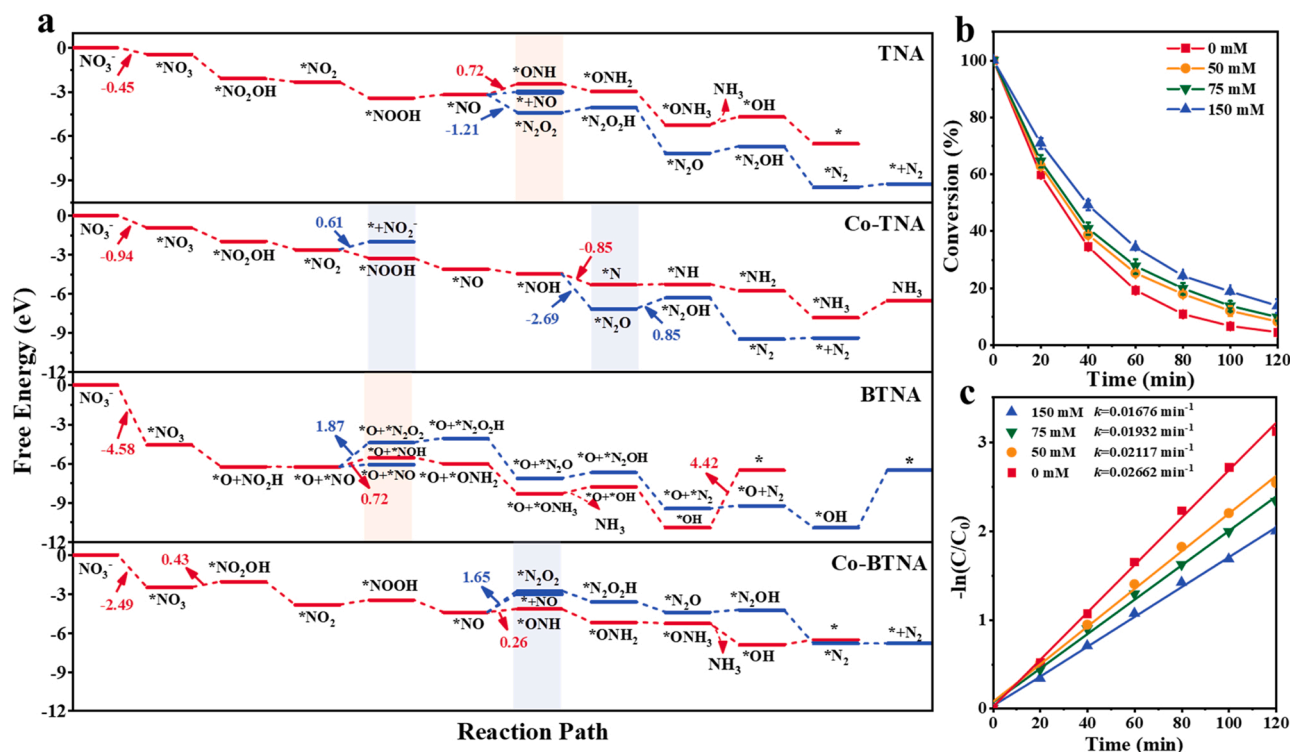
Fig. 9. : Free energy diagrams of NO_3^- reduction on TNA, BTNA, Co-TNA and Co-BTNA (a). The change of NO_3^- residual during NRA process on Co-BNTA with different addition concentration of TBA (b). The linearized pseudo first-order kinetic profiles of Co-BTNA with different addition concentration of TBA (c).

27.1 kwh·kg^{-1}, and realizing zero addition of reagents. The activity and NH_3 selectivity of Co-BNTA remained reliable after at least ten recycling tests (Fig. S18), while the cathode bias during the ERRNA operation induced the increase of the content of OVs and led to further self-optimization of the catalytic performance. The results presented here open a new avenue for the design and construction of membrane electrode assembly devices for the direct production of valuable ammonia products from wastewater without external chemical addition.

CRediT authorship contribution statement

Qi Zhang conceived the experiments and wrote the initial manuscript; **Qi Zhang** and **Yifan Li** performed DFT calculations. **Mengnan Geng** and **Juntao Zhu** contributed to the discussion. **Yifan Li, Haofen Sun** and **Bo Jiang** contributed to data analyses and wrote the final manuscript. All authors read and agreed the manuscript. **Bo Jiang** and **Yifan Li** coordinated the project.

Declaration of Competing Interest

The authors declare that they have no known competing financial interests or personal relationships that could have appeared to influence the work reported in this paper.

Data availability

Data will be made available on request.

Acknowledgments

Author Contributions

Qi Zhang conceived the experiments and wrote the initial manuscript; Qi Zhang and Yifan Li performed DFT calculations. Juntao Zhu and Mengnan Geng contributed to the discussion. Yifan Li, Haofen Sun and Bo Jiang contributed to data analyses and wrote the final manuscript. All authors read and agreed the manuscript. Bo Jiang and Yifan Li coordinated the project.

Appendix A. Supporting information

Supplementary data associated with this article can be found in the online version at doi:10.1016/j.apcatb.2023.122658.

References

[1] J.G. Chen, R.M. Crooks, L.C. Seefeldt, K.L. Bren, R.M. Bullock, M.Y. Darensbourg, P.L. Holland, B. Hoffman, M.J. Janik, A.K. Jones, Beyond fossil fuel-driven nitrogen transformations, Science 360 (2018), eaar6611.

[2] I. Rafiqul, C. Weber, B. Lehmann, A. Voss, Energy efficiency improvements in ammonia production-perspectives and uncertainties, Energy 30 (2005) 2487–2504.

[3] Z.W. Seh, J. Kibsgaard, C.F. Dickens, I. Chorkendorff, J.K. Nørskov, T.F. Jaramillo, Combining theory and experiment in electrocatalysis: insights into materials design, Science 355 (2017), eaad4998.

[4] F.D. Belkada, O. Kitous, N. Drouiche, S. Aoudj, O. Bouchelaghem, N. Abdi, H. Grib, N. Mameri, Electrodialysis for fluoride and nitrate removal from synthesized photovoltaic industry wastewater, Sep. Purif. Technol. 204 (2018) 108–115.

[5] H. Yoshino, Y. Kawase, Kinetic modeling and simulation of zero-valent iron wastewater treatment process: simultaneous reduction of nitrate, hydrogen peroxide, and phosphate in semiconductor acidic wastewater, Ind. Eng. Chem. Res. 52 (2013) 17829–17840.

[6] R. King, N. Bhattacharyya, H. Smith, K. Wiemers, Noble metal-catalyzed homogeneous and heterogeneous processes in treating simulated nuclear waste media with formic acid, J. Mol. Catal. A-Chem. 107 (1996) 145–152.

[7] X. Huo, J. Vanneste, T.Y. Cath, T.J. Strathmann, A hybrid catalytic hydrogenation/ membrane distillation process for nitrogen resource recovery from nitrate-contaminated waste ion exchange brine, Water Res. 175 (2020), 115688.

[8] N. Gruber, J.N. Galloway, An Earth-system perspective of the global nitrogen cycle, Nature 451 (2008) 293–296.

[9] I. Mikami, Y. Sakamoto, Y. Yoshinaga, T. Okuhara, Kinetic and adsorption studies on the hydrogenation of nitrate and nitrite in water using Pd-Cu on active carbon support, Appl. Catal. B- Environ. 44 (2003) 79–86.

[10] G. Dima, A. De Vooys, M. Koper, Electrocatalytic reduction of nitrate at low concentration on coinage and transition-metal electrodes in acid solutions, J. Electro Chem. 554 (2003) 15–23.

[11] A. De Vooys, R. Van Santen, J. Van Veen, Electrocatalytic reduction of NO_3^- on palladium/copper electrodes, J. Mol. Catal. A-Chem. 154 (2000) 203–215.

[12] T. Chen, H. Li, H. Ma, M.T. Koper, Surface modification of Pt (100) for electrocatalytic nitrate reduction to dinitrogen in alkaline solution, Langmuir 31 (2015) 3277–3281.

[13] Y. Yang, L.C. Kao, Y. Liu, K. Sun, H. Yu, J. Guo, S.Y.H. Liou, M.R. Hoffmann, Cobalt-doped black TiO2 nanotube array as a stable anode for oxygen evolution and electrochemical wastewater treatment, ACS Catal. 8 (2018) 4278–4287.

[14] Y. Yang, M.R. Hoffmann, Synthesis and stabilization of blue-black TiO_2 nanotube arrays for electrochemical oxidant generation and wastewater treatment, Environ. Sci. Technol. 50 (2016) 11888–11894.

[15] X. Ma, M. Li, C. Feng, W. Hu, L. Wang, X. Liu, Development and reaction mechanism of efficient nano titanium electrode: reconstructed nanostructure and enhanced nitrate removal efficiency, J. Electroanal. Chem. 782 (2016) 270–277.

[16] F. Fabregat-Santiago, E.M. Barea, J. Bisquert, G.K. Mor, K. Shankar, C.A. Grimes, High carrier density and capacitance in TiO_2 nanotube arrays induced by electrochemical doping, J. Am. Chem. Soc. 130 (2008) 11312–11316.

[17] R. Jia, Y. Wang, C. Wang, Y. Ling, Y. Yu, B. Zhang, Boosting selective nitrate electroreduction to ammonium by constructing oxygen vacancies in TiO_2, ACS Catal. 10 (2020) 3533–3540.

[18] D. Pak, Ti plate with TiO_2 nanotube arrays as a novel cathode for nitrate reduction, Chemosphere 228 (2019) 611–618.

[19] Y. Fang, Q. Zhang, H. Zhang, X. Li, W. Chen, J. Xu, H. Shen, J. Yang, C. Pan, Y. Zhu, Dual activation of molecular oxygen and surface lattice oxygen in single atom Cu^1/ TiO_2 catalyst for COO, Angew. Chem. Int. Ed. (2022).

[20] J. Lim, Y. Yang, M.R. Hoffmann, Activation of peroxymonosulfate by oxygen vacancies-enriched cobalt-doped black TiO_2 nanotubes for the removal of organic pollutants, Environ. Sci. Technol. 53 (2019) 6972–6980.

[21] N. Zhang, C. Gao, Y. Xiong, Defect engineering: a versatile tool for tuning the activation of key molecules in photocatalytic reactions, J. Energy Chem. 37 (2019) 43–57.

[22] H. Huang, F. Li, Q. Xue, Y. Zhang, S. Yin, Y. Chen, Salt-templated construction of ultrathin cobalt doped iron thiophosphite nanosheets toward electrochemical ammonia synthesis, Small 15 (2019) 1903500.

[23] J. Wang, C. Cai, Y. Wang, X. Yang, D. Wu, Y. Zhu, M. Li, M. Gu, M. Shao, Electrocatalytic reduction of nitrate to ammonia on low-cost ultrathin CoOx nanosheets, ACS Catal. 11 (2021) 15135–15140.

[24] X. Zhang, Y. Wang, C. Liu, Y. Yu, S. Lu, B. Zhang, Recent advances in non-noble metal electrocatalysts for nitrate reduction, Chem. Eng. J. 403 (2021), 126269.

[25] J. Gao, N. Shi, X. Guo, Y. Li, X. Bi, Y. Qi, J. Guan, B. Jiang, Electrochemically selective ammonia extraction from nitrate by coupling electron-and phase-transfer reactions at a three-phase interface, Environ. Sci. Technol. 55 (2021) 10684–10694.

[26] M. Paulose, K. Shankar, S. Yoriya, H.E. Prakasam, O.K. Varghese, G.K. Mor, T. A. Latempa, A. Fitzgerald, C.A. Grimes, Anodic growth of highly ordered TiO_2 nanotube arrays to 134 μm in length, J. Phys. Chem. B 110 (2006) 16179–16184.

[27] W. Teng, N. Bai, Y. Liu, Y. Liu, J. Fan, W.-x Zhang, Selective nitrate reduction to dinitrogen by electrocatalysis on nanoscale iron encapsulated in mesoporous carbon, Environ. Sci. Technol. 52 (2018) 230–236.

[28] M. Segall, R. Shah, C.J. Pickard, M. Payne, Population analysis of plane-wave electronic structure calculations of bulk materials, Phys. Rev. B 54 (1996), 16317.

[29] J.P. Perdew, K. Burke, M. Ernzerhof, Generalized gradient approximation made simple, Phys. Rev. Lett. 77 (1996) 3865.

[30] J.K. Nørskov, T. Bligaard, A. Logadottir, J. Kitchin, J.G. Chen, S. Pandelov, U. Stimming, Trends in the exchange current for hydrogen evolution, J. Electrochem. Soc. 152 (2005) J23.

[31] E. Paek, A.J. Pak, G.S. Hwang, A computational study of the interfacial structure and capacitance of graphene in [BMIM][PF6] ionic liquid, J. Electrochem. Soc. 160 (2012) A1.

[32] A.J. Pak, E. Paek, G.S. Hwang, Tailoring the performance of graphene-based supercapacitors using topological defects: a theoretical assessment, Carbon 68 (2014) 734–741.

[33] Y. Wang, A. Xu, Z. Wang, L. Huang, J. Li, F. Li, J. Wicks, M. Luo, D.-H. Nam, C.- S. Tan, Enhanced nitrate-to-ammonia activity on copper-nickel alloys via tuning of intermediate adsorption, J. Am. Chem. Soc. 142 (2020) 5702–5708.

[34] J.-X. Liu, D. Richards, N. Singh, B.R. Goldsmith, Activity and selectivity trends in electrocatalytic nitrate reduction on transition metals, ACS Catal. 9 (2019) 7052–7064.

[35] G. Dima, G. Beltramo, M. Koper, Nitrate reduction on single-crystal platinum electrodes, Electrochim. Acta 50 (2005) 4318–4326.

[36] M. Cerro-Lopez, Y. Meas-Vong, M. Méndez-Rojas, C. Martínez-Huitle, M. Quiroz, Formation and growth of PbO_2 inside TiO_2 nanotubes for environmental applications, Appl. Catal. B- Environ. 144 (2014) 174–181.

[37] A. Chanda, K. Rout, M. Vasundhara, S.R. Joshi, J. Singh, Structural and magnetic study of undoped and cobalt doped TiO_2 nanoparticles, RSC Adv. 8 (2018) 10939–10947.

[38] L. Chen, X. Zuo, S. Yang, T. Cai, D. Ding, Rational design and synthesis of hollow Co_3O_4@ Fe_2O_3 core-shell nanostructure for the catalytic degradation of norfloxacin by coupling with peroxymonosulfate, Chem. Eng. J. 359 (2019) 373–384.

[39] Y. Liang, Y. Li, H. Wang, J. Zhou, J. Wang, T. Regier, H. Dai, Co_3O_4 nanocrystals on graphene as a synergistic catalyst for oxygen reduction reaction, Nat. Mater. 10 (2011) 780–786.

[40] Y. Yang, S. Zhang, S. Wang, K. Zhang, H. Wang, J. Huang, S. Deng, B. Wang, Y. Wang, G. Yu, Ball milling synthesized MnOx as highly active catalyst for gaseous POPs removal: significance of mechanochemically induced oxygen vacancies, Environ. Sci. Technol. 49 (2015) 4473–4480.

[41] G. Lu, A. Linsebigler, J.T. Yates Jr, The adsorption and photodesorption of oxygen on the TiO_2 (110) surface, J. Chem. Phys. 102 (1995) 4657–4662.

[42] D.D. Babu, Y. Huang, G. Anandhababu, X. Wang, R. Si, M. Wu, Q. Li, Y. Wang, J. Yao, Atomic iridium@ cobalt nanosheets for dinuclear tandem water oxidation, J. Mat. Chem. A 7 (2019) 8376–8383.

[43] Y. Ji, J. Niu, D. Xu, K. Wang, J. Brejcha, S. Jeon, D.M. Warsinger, Efficient electrocatalysis for denitrification by using TiO_2 nanotube arrays cathode and adding chloride ions, Chemosphere 274 (2021), 129706.

[44] A. Jain, S.P. Ong, G. Hautier, W. Chen, W.D. Richards, S. Dacek, S. Cholia, D. Gunter, D. Skinner, G. Ceder, Commentary: the materials project: a materials genome approach to accelerating materials innovation, APL Mater. 1 (2013), 011002.

[45] J. Lim, D. Monllor-Satoca, J.S. Jang, S. Lee, W. Choi, Visible light photocatalysis of fullerol-complexed TiO2 enhanced by Nb doping, Appl. Catal. B-Environ. 152 (2014) 233–240.

[46] J. Gao, B. Jiang, C. Ni, Y. Qi, Y. Zhang, N. Oturan, M.A. Oturan, Non-precious Co_3O_4-TiO_2/Ti cathode based electrocatalytic nitrate reduction: preparation, performance and mechanism, Appl. Catal. B-Environ. 254 (2019) 391–402.

[47] D. Hou, A. Iddya, X. Chen, M. Wang, W. Zhang, Y. Ding, D. Jassby, Z.J. Ren, Nickel-based membrane electrodes enable high-rate electrochemical ammonia recovery, Environ. Sci. Technol. 52 (2018) 8930–8938.

[48] F. Yin, H. Liu, The j-pH diagram of interfacial reactions involving H^+ and OH^-, J. Energy Chem. 50 (2020) 339–343.

[49] C. Zhang, J. Ma, J. Song, C. He, T.D. Waite, Continuous ammonia recovery from wastewaters using an integrated capacitive flow electrode membrane stripping system, Environ. Sci. Technol. 52 (2018) 14275–14285.

[50] A. Kapałka, S. Fierro, Z. Frontistis, A. Katsaounis, S. Neodo, O. Frey, N. De Rooij, K. M. Udert, C. Comninellis, Electrochemical oxidation of ammonia (NH_4^+/NH_3) on thermally and electrochemically prepared IrO_2 electrodes, Electrochim. Acta 56 (2011) 1361–1365.

[51] C. Zhang, D. He, J. Ma, T.D. Waite, Active chlorine mediated ammonia oxidation revisited: reaction mechanism, kinetic modelling and implications, Water Res. 145 (2018) 220–230.

[52] J. Dykstra, P. Biesheuvel, H. Bruning, A. Ter Heijne, Theory of ion transport with fast acid-base equilibrations in bioelectrochemical systems, Phys. Rev. E 90 (2014), 013302.

[53] K.-Y. Kim, D.A. Moreno-Jimenez, H. Efstathiadis, Electrochemical ammonia recovery from anaerobic centrate using a nickel-functionalized activated carbon membrane electrode, Environ. Sci. Technol. 55 (2021) 7674–7680.